Controlled Assembly of Biodegradable Plasmonic Nanoclusters for Near-Infrared Imaging and Therapeutic Applications

Jasmine M. Tam,[†,‖] Justina O. Tam,[‡,‖] Avinash Murthy,[†] Davis R. Ingram,[†] Li Leo Ma,[†] Kort Travis,[§] Keith P. Johnston,[†,*] and Konstantin V. Sokolov[‡,⊥,*]

[†]Department of Chemical Engineering, [‡]Department of Biomedical Engineering, and [§]Department of Physics, University of Texas at Austin, Austin, Texas 78712, and [⊥]Department of Imaging Physics, M.D. Anderson Cancer Center, Houston, Texas 77030. [‖]These authors contributed equally to this work.

ABSTRACT Metal nanoparticles with surface plasmon resonance (SPR) in the near-infrared region (NIR) are of great interest for imaging and therapy. Presently, gold nanoparticles with NIR absorbance are typically larger than 50 nm, above the threshold size of ∼5 nm required for efficient renal clearance. As these nanoparticles are not biodegradable, concerns about long-term toxicity have restricted their translation into the clinic. Here, we address this problem by developing a flexible platform for the kinetically controlled assembly of sub-5 nm ligand-coated gold particles to produce metal/polymer biodegradable nanoclusters smaller than 100 nm with strong NIR absorbance for multimodal application. A key novel feature of the proposed synthesis is the use of weakly adsorbing biodegradable polymers that allows tight control of nanocluster size and, in addition, results in nanoclusters with unprecedented metal loadings and thus optical functionality. Over time, the biodegradable polymer stabilizer degrades under physiological conditions that leads to disassembly of the nanoclusters into sub-5 nm primary gold particles which are favorable for efficient body clearance. This synthesis of polymer/inorganic nanoclusters combines the imaging contrast and therapeutic capabilities afforded by the NIR-active nanoparticle assembly with the biodegradability of a polymer stabilizer.

*Address correspondence to
kostia@mail.utexas.edu,
kpj@che.utexas.edu.

Various plasmonic particles including nanoshells,[1−3] nanorods,[4] nanocages,[5,6] and nanoroses,[7] which scatter and absorb in the NIR region (650−900 nm), where soft tissues and blood are most transparent, can be used for molecular-specific imaging, therapy, and multimodal applications.[1,4,5,7−11] Intravenous administration of nanoparticles provides an effective method for rapid delivery throughout the body. In general, particles with dimensions between 6 and 100 nm exhibit sufficiently long blood residence times for accumulation at disease sites such as cancer and cardiovascular plaques.[12−15] Particles smaller than ∼6 nm can be removed too rapidly by the kidneys to be effective for imaging and therapy,[16] whereas particles larger than 100 nm become more susceptible for clearance from the circulation by the spleen.[17] Within this size range, plasmonic nanoparticles with larger geometrical dimensions have stronger optical cross sections that are advantageous for imaging and therapy. Presently, metal nanoparticles with strong NIR absorbance are typically larger than 50 nm.[1,4,5,18−20] As these inorganic particles are not biodegradable, concerns about long-term toxicity[16,21] have restricted their translation into the clinic. The safe translation of plasmonic nanoparticles to clinical practice for systemic targeting of diseases would require efficient clearance of the particles from the body. Previous studies strongly indicate that nanoparticles with sizes less than ∼6 nm are needed to achieve this goal.[16] Thus, this dilemma in the particle size needed for delivery, imaging, and therapy *versus* efficient body clearance creates a serious conflict in biomedical applications of NIR-absorbing plasmonic nanoparticles.

Here, we address this problem by developing a flexible platform for the kinetically controlled assembly of sub-5 nm gold particles to produce ∼100 nm biodegradable nanoclusters with strong NIR absorbance for multimodal application. The nanoclusters are stabilized with a small amount of a weakly adsorbed biodegradable triblock copolymer of polylactic acid and polyethylene glycol, PLA(2K)-*b*-PEG(10K)-*b*-PLA(2K). The polymer degrades under physiological conditions to release the constituent clearable gold nanoparticles. These clusters can provide sufficient blood residence time for clinical application, while facilitating effective clearance from the body after biodegradation (Figure 1a). The close spacing between gold nanoparticles within the 100 nm clusters, resulting from the small amount of polymer, which is located primarily near the exterior cluster
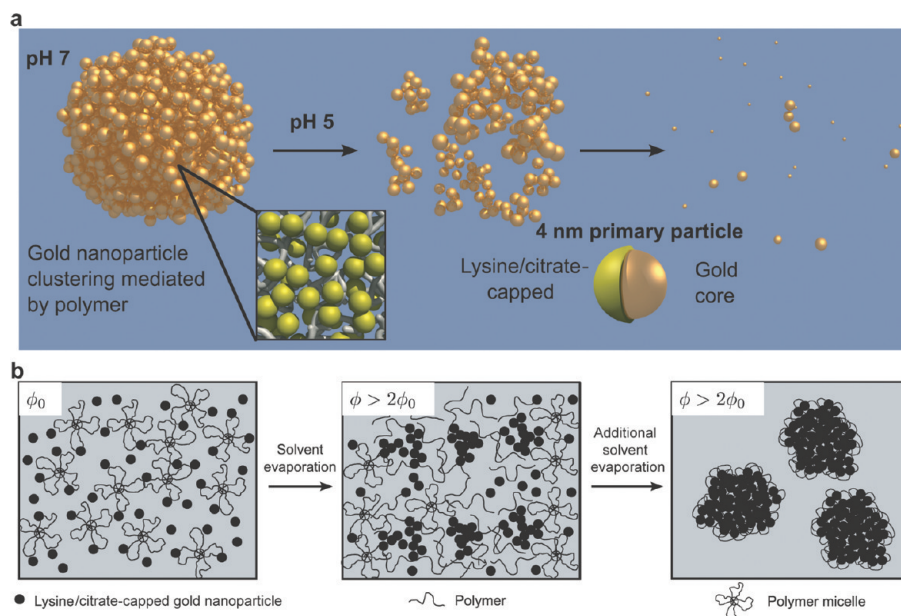
Figure 1. Schematic of synthesis and degradation of gold nanoclusters. (a) Illustration of a biodegradable nanocluster, which is composed of ~4 nm primary gold particles held together with a biodegradable polymer. Upon polymer degradation, catalyzed by low pH in endosomal compartments of cells, the nanocluster deaggregates into primary gold nanoparticles. (b) Schematic of nanocluster formation process, in which primary gold nanoparticles aggregate in the presence of a polymer in a controlled manner to yield sub-100 nm clusters. Polymer adsorption to the nanoparticle surface and an increase in the volume fraction of particles, φ, *via* solvent evaporation promote cluster formation.

surface, facilitates strong NIR scattering and absorption. The PEG loops in the center block of the polymer extend into the aqueous environment and provide steric stabilization for the clusters.

RESULTS AND DISCUSSION

Nanocluster size and physical properties, especially interparticle spacing, are controlled by varying particle volume fractions during solvent evaporation. The changes in electrostatic, van der Waals (VDW), depletion, and steric interactions upon the concentration of the gold nanoparticles and polymer micelles govern the kinetic assembly of the nanoclusters, as well as their disassembly after polymer degradation. Without the presence of a polymeric stabilizer, irregular micrometer-sized aggregates of gold nanoparticles have been formed by varying the particle charge upon adjusting pH, for particles capped with lysine,[22,23] cysteine,[24] or glutathione[25] ligands. Alternatively, nanoclusters of
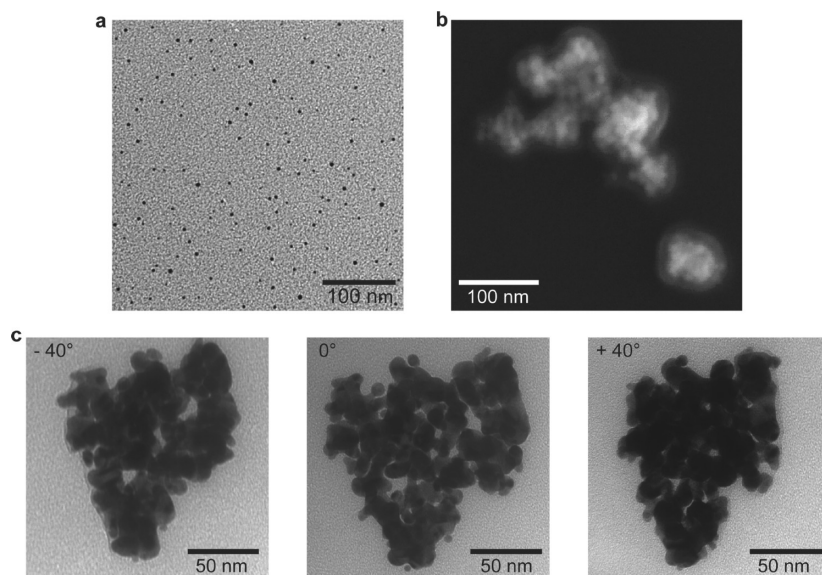

Figure 2. Electron microscopy characterization of gold nanoclusters. (a) TEM of initial 4 nm lysine/citrate-capped gold nanoparticles before clustering. (b) SEM and (c) TEM micrographs of nanoclusters templated using PLA(2K)-PEG(10K)-PLA(2K) at a 16/1 polymer/Au ratio (w/w). For TEM micrographs, the stage was tilted at an angle of −40, 0 (no tilt), and 40°.

TABLE 1. Characterization of Gold Primary Particles and Nanoclusters[a]

ligand	absorbance (750 nm)	$D_{avg,primary particle}$ (nm)	$D_{avg,cluster,pH=7.4}$ (nm)	$D_{avg,deag,pH=5}$ (nm)
lysine/citrate	1.10	4.1 ± 0.8	83.0 ± 4.6	4.4 ± 0.8
citrate	1.09	4.0 ± 0.8	119.4 ± 22.5	4.0 ± 0.9

[a]Absorbance measurements were recorded at gold concentrations of ~56 μg/mL. All nanoclusters were formed at 100% evaporation using the polymer PLA(2K)-b-PEG(10K)-b-PLA(2K). Average hydrodynamic diameters, D_{avg}, for nanoclusters were determined by DLS. D_{avg} for primary particles and deaggregated particles ($D_{avg,deag}$) were measured by image analysis of TEM micrographs.

metals may be formed by equilibrium self-assembly with polymer templates.[26−28] However, the high polymer concentrations required for the equilibrium assembly lead to metal loadings and interparticle spacings that are not sufficient for strong NIR absorbance. Additionally, the templating agents are highly specialized. In contrast, our kinetically controlled assembly platform requires only small concentrations of common copolymers as stabilizers and simple biocompatible capping ligands on gold, such as citrate and/or lysine.

Cluster growth is controlled through mediation of the interactions between ligand-capped gold particles with the biodegradable polymer, as shown in Figure 1b. Gold nanoparticles stabilized with citrate ligands were synthesized based on a previously published method.[29] A solution of 1% lysine in pH 8.4 phosphate buffer (10 mM) was added to 1.2 mL of a 3.0 mg/mL colloidal gold solution to yield a final lysine concentration of 0.4 mg/mL and an average diameter of 4.1 ± 0.8 nm (Figure 2a and Table 1). The dispersion was stirred for 12 h.[23] PLA(2K)-PEG(10K)-PLA(2K) (Sigma Aldrich Co., St. Louis, MO) (60 mg) was added to the aqueous gold dispersion, yielding a final polymer concentration of 50 mg/mL. The dispersion was sonicated in a bath sonicator for 5 min, during which the dispersion changed from ruby red color to a darker red-purple color. Upon evaporation of ~80% of the solvent, the dispersion turned blue, indicating absorption in the red. Complete solvent evaporation over 2 h produced a smooth blue film. Reconstitution of the film with deionized (DI) water to a concentration of ~0.3 mg/mL yielded a dark blue dispersion. The fact that this dispersion consists of sub-100 nm clusters composed of primary gold nanoparticles is indicated by scanning electron (SEM) and transmission election microscopy (TEM) (Figure 2). TEM images taken at various angles reveal closely spaced primary gold nanoparticles throughout the porous cluster. The average hydrodynamic diameter measured by dynamic light scattering (DLS) was 83.0 ± 4.6 nm (Figure 3a and Table 1), in agreement with the TEM results. In the SEM image (Figure 2b), a polymer-rich shell a few nanometers thick is apparent on the exterior of the clusters, which potentially provides steric stabilization of the dispersion.

Thermogravimetric analysis indicated that the nanoclusters contained only 20 ± 5% organic material (poly-
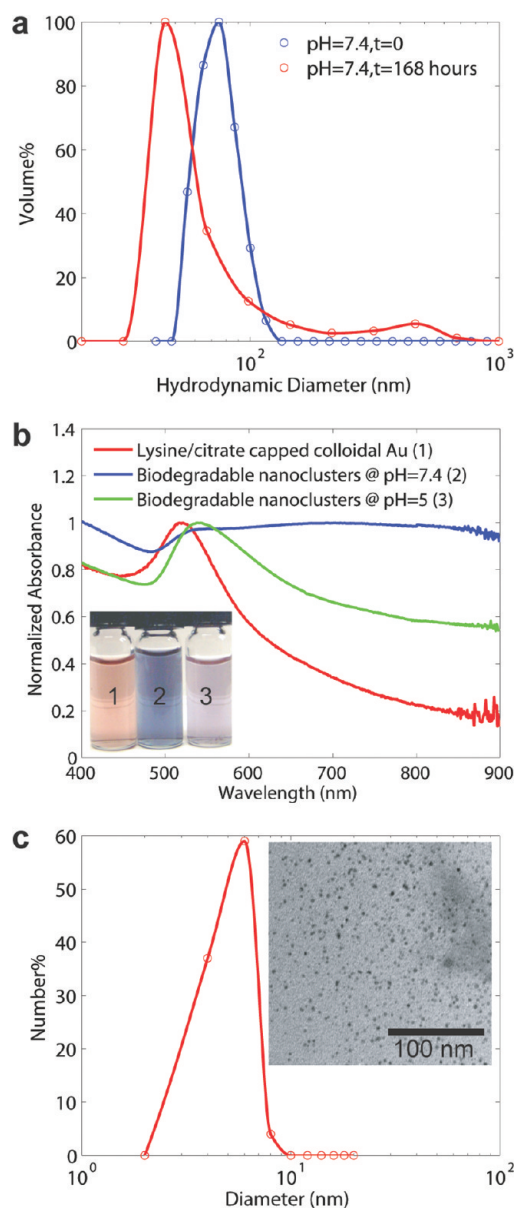

Figure 3. Degradation of gold nanoclusters in solution. (a) Hydrodynamic diameter (DLS) in pH 7.4 media initially and after 168 h (1 week) of incubation. (b) UV−vis−NIR absorbance spectra of (1) colloidal dispersion of lysine/citrate-capped gold nanoparticles, (2) biodegradable nanoclusters (pH = 7.4), and (3) deaggregated nanoclusters (pH = 5). (c) Size distribution after deaggregation in pH = 5 media, as determined by image analysis of TEM micrographs (>200 particles). Inset: TEM micrograph of nanoclusters after incubation at pH = 5 for 1 week.

mer and ligands), 10−15% of which was polymer. These low polymer loadings allow close spacing of the gold primary particles. Interparticle distances between constituent gold particles within the cluster were estimated to be 1.80 ± 0.6 nm based on the more discernible particles in the periphery of TEM images (Supporting Information Figure S1). This spacing is consistent with the length scale of a lysine−lysine dipeptide in solution of 1.49 nm.[22] The ability to simultaneously control cluster size and spacing of gold nanoparticles within the nanocluster was achieved through manipulation of particle volume fractions upon solvent evaporation, as well as control of the electrostatic, VDW, depletion, and steric interactions between the gold primary particles and the polymer (see Supporting Information). This approach provides greater control over the nanocluster morphology, relative to nanoclusters formed during reduction of gold precursors without a polymer stabilizer.[30,31] Control of the depletion interactions, along with the propensity of hydrophilic PEG blocks to migrate to the exterior of the clusters at the interface with water, facilitates low polymer loadings within the clusters.

Optical extinction spectra changed markedly upon cluster formation as shown in Figure 3b. The initial dispersion of gold nanoparticles had a maximum absorbance at 520 nm, which is characteristic of isolated gold spheres. The blue nanocluster dispersion had a broad, relatively constant absorbance in the NIR region from 700 to 900 nm. The extinction coefficient at the maximum absorbance, ε_{703}, was 0.020 cm^2/µg of gold for a 56 µg/mL gold dispersion. When it is assumed that the gold nanoparticles are in a closest packed state (based on SEM and TEM images in Figure 2b,c), the estimated nanocluster extinction cross section was ∼10^{-14} m^2 (see Supporting Information), comparable to the value for nanoshells,[1,8] nanocages,[5] nanorods,[8] and nanoroses.[7] The high NIR absorbance observed for nanoclusters may be attributed to a combination of the following factors: close interparticle spacing between constituent gold nanoparticles, non-uniform spatial distribution of the constituent particles within the nanocluster, roughness of the nanocluster boundary surface, and finally, any deviation in the overall aspect ratio of the entire nanocluster from that of a sphere. The close spacing between gold particles is well within the fraction of the particle diameter known to produce significant red shift in the SPR.[8,32−37] TEM images (Figure 2) also show that short oligomers of primary particles and subcluster domains can be clearly observed, indicative of a non-uniform volume-packing distribution of the constituent particles. When combined with strong plasmonic coupling, this non-uniform distribution significantly enhances the red shift of the SPR.[8,34] The NIR absorbance per total particle mass is much higher compared to previous composite particles with smaller amounts of gold nanoparticles templated with liposomes, block copolymer micelles, or DNA.[26,28,38]

Nanoclusters with strong NIR absorbance were also produced by clustering more negatively charged citrate-capped gold nanoparticles, which possess a ζ potential of −44.0 ± 4.9 mV, compared to −30.1 ± 2.4 mV for the lysine/citrate-capped nanoparticles (Table 1). The remainder of the paper will focus on the lysine/citrate-capped nanoclusters due to their slightly smaller sizes.

The initial stability and degradation of the nanoclusters were examined at pH 7.4 and 5, simulating normal cellular environments and the interior of cellular lysosomes, respectively.[39] After storage for 1 week in pH 7.4 buffer, the DLS peak shifted modestly toward smaller sizes (Figure 3a). This limited degradation is consistent with the long half-life of PLA (MW = 2000) of about 4 weeks at neutral pH. In contrast, upon incubation at pH 5, upon addition of 0.1 N HCl, for 1 week, nearly complete nanocluster deaggregation was observed by TEM (Figure 3c and Table 1). The mean particle size of the deaggregated particles was 4.3 ± 0.1 nm (over 100 particles analyzed), comparable to the initial size of the ligand-capped gold particles of 4.1 ± 0.8 nm (Supporting Information Figure S2). Upon degradation of the polymer, a combination of steric repulsion due to the capping ligands and remaining polymer fragments, electrostatic repulsion due to the negative charge of the gold particles, and effective entropic forces are sufficient to completely redisperse the primary gold particles. The associated extinction spectra undergo a substantial shift toward the original spectrum of the colloidal gold spheres, and the color of the dispersion changes back toward red (Figure 3b). The remaining discrepancy between these spectra is attributed to the presence of a small number of clusters (7%) still present in the dispersion. Deaggregation to constituent nanoparticles was also observed for the clusters produced using citrate-only capped nanoparticles (Table 1).

Nanocluster biodegradation was also assessed in a murine macrophage cell line (J477A.1, American Type Culture Collection, Manassas, VA). Scattering spectra from hypespectral images of cells (Figure 4a,c), darkfield reflectance (DR) (Figure 4b,d, top row), and hyperspectral (HS) images (Figure 4b,d, bottom row) were acquired at 24, 96, and 168 h time points after cells were treated with nanoclusters. High nanocluster uptake was evident in the DR images, where nanoclusters strongly scattered illumination light; overall scattering intensity decreased over time as macrophages divided and nanoclusters were distributed between daughter cells (Figure 4b, top row). A significant increase in the red-NIR scattering signal of the labeled cells was seen compared to unlabeled cells (compare Figure 4a, dark blue curve, and c), consistent with the high scattering efficiency of the nanoclusters in solution (Figure 4a, light blue curve). The relative intensity of the red-NIR scattering signal decreased after 96 h, and the scattering from labeled cells showed a marked blue shift to
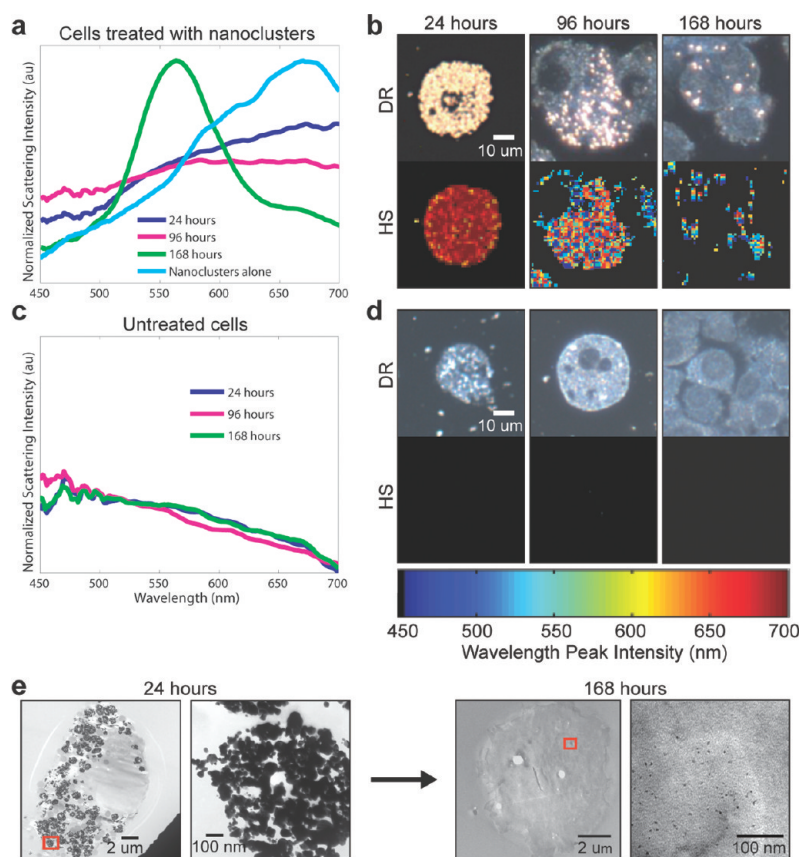
Figure 4. Biodegradation of gold nanoclusters inside live cells. Scattering spectra (normalized by area under the curve) of (a) live cells labeled with nanoclusters and (c) control cells without nanoclusters. The spectra were taken at 24, 96, and 168 h time points after cells were treated with nanoclusters. Dark-field reflectance (DR) images of cells treated with (b) nanoclusters and (d) control cells over time are shown together with corresponding color coded images indicating scattering peak position at each pixel in the field of view (b and d, bottom rows). Hyperspectral (HS) images and the color bar were used to obtain the color coded distribution of scattering peaks within cells (b and d, bottom row). Pixels that did not have an identifiable peak in a corresponding spectrum were not assigned a color. The scale bar in the DR and HS images is 10 μm. (e) TEM images of cells treated with nanoclusters at low magnification (scale bar 2 μm) and high magnification (scale bar 100 nm) at 24 and 168 h. Red boxes in the low magnification images are magnified on the right at each time point.

~550 nm that is consistent with scattering from the constituent lysine/citrate-capped gold nanoparticles (Supporting Information Figure S3). Hyperspectral images showed a gradual progression from very strong scattering in the 650−700 nm region at $t = 24$ h to a less intense scattering signal predominantly in the 500−550 nm region at $t = 168$ h (Figure 4b, bottom row). The endogenous scattering for the control cells did not significantly change with time (Figure 4c,d). Note that scattering from the control cells is approximately 6 times weaker compared to the labeled cells. In addition, most of the pixels in the hyperspectral images of untreated cells do not exhibit any distinct scattering peaks that result in black appearance of the images in Figure 4d, bottom row.

The biodegradation of nanoclusters inside live cells was further confirmed by TEM (Figure 4e). After 24 h, large ~100 nm nanoclusters can be observed throughout the interior of cells (Figure 4e, 24 h), whereas after 168 h, cells contain only particles less than 5 nm in diameter (Figure 4e, 168 h). These TEM results are in excellent agreement with

optical measurements and with deaggregation results in solution, providing unambiguous proof of essentially complete biodegradation of the initial ~100 nm nanoclusters into sub-5 nm primary particles (Supporting Information Figure S2).

CONCLUSIONS

In this study, we developed a general kinetic assembly platform for the design of hybrid polymer/gold nanoclusters smaller than 100 nm with closely spaced gold spheres that produce strong absorbance in the NIR. Only small amounts of biodegradable polymers are required to reduce electrostatic repulsion between the gold particles to stabilize the clusters. These nanoclusters can simultaneously provide strong optical cross sections required for imaging and therapy, prolonged blood residence time required for effective systemic delivery, and degradation to small sizes required for effective clearance from the body. The presented method is readily generalizable, for example, to gold particles with varying surface chemistries, which play an im-

portant role in clearance, or to multiple types of primary particles to allow multiplexing for multimodal and multifunctional applications. In combination, all of these benefits will facilitate the translation of plasmonic nanoparticle applications into clinical practice.

METHODS

Gold Particle Synthesis: To synthesize the citrate-capped gold nanoparticles, 100 mL of DI water was heated to 97 °C. While stirring, 1 mL of 1% $HAuCL_4 \cdot 3H_2O$, 1 mL of 1% $Na_3C_3H_5O(COO)_3 \cdot 2H_2O$, and 1 mL of 0.075% $NaBH_4$ in a 1% $Na_3C_3H_5O(COO)_3 \cdot 2H_2O$ solution was added in 1 min intervals. The solution was stirred for 5 min and then removed to an ice bath to cool to room temperature. The gold particles were then concentrated using centrifugal filter devices (Ultracel YM-30, Millipore Co.) to 3.0 mg Au/mL. Gold concentrations were determined using flame atomic absorption spectroscopy (FAAS), as described below.

Nanocluster Characterization: The nanocluster morphology was observed by scanning electron (SEM) and transmission electron microscopy (TEM). A Zeiss Supra 40VP field emission SEM was operated at an accelerating voltage of 5−10 kV. SEM samples were prepared by depositing a dilute aqueous dispersion of the nanoclusters onto a silicon wafer. The sample was dried and washed with DI water to remove excess polymer. TEM was performed on a FEI TECNAI G2 F20 X-TWIN TEM using a high-angle annular dark-field detector. A dilute aqueous dispersion of the nanoclusters was deposited onto a 200 mesh carbon-coated copper TEM grid for observation. Separation distances between primary particles within the nanoclusters were measured by analyzing TEM images using Scion Image software (Frederick, Maryland). UV−vis spectra were obtained with a Varian Cary 5000 spectrophotometer and a 1 cm path length. Dynamic light scattering (DLS) measurements of hydrodynamic diameter and ζ potential measurements were performed in triplicate on a Brookhaven Instruments ZetaPlus dynamic light scattering apparatus (scattering angle of 90°) at a temperature of 25 °C. Dispersion concentrations were adjusted with either DI water for DLS measurements or pH = 7.4 buffer (10 mM) for ζ potential measurements to yield a measured count rate between 300 and 400 kcps. Prior to all DLS measurements, the nanocluster dispersions were filtered through a 0.2 μm filter and probe sonicated for 2 min. Data analysis was performed using a digital autocorrelator (Brookhaven BI-9000AT) with a non-negative least-squares (NNLS) method (Brookhaven 9KDLSW32). Reported average diameters correspond to the D_{50} or diameter at which the cumulative sample volume was under 50%. For ζ potential measurements, the average value of at least three data points was reported. Thermogravimetric analysis (TGA) was conducted using a Perkin-Elmer TGA 7 under nitrogen atmosphere at a gas flow rate of 20 mL/min. The samples were cleaned to remove excess polymer by centrifuging nanocluster dispersions at 8000 rpm for 5 min at 4 °C. TGA samples were heated at a constant rate of 20 °C/min from 30 to 800 °C and then held at 800 °C for 30 min. Flame atomic absorption spectroscopy (FAAS) was used to determine the gold concentration in the nanocluster dispersions using a GBC 908AA flame atomic absorption spectrometer (GBC Scientific Equipment Pty Ltd.). Measurements were conducted at 242.8 nm using an air-acetylene flame. To determine clustering efficiency, a dispersion of nanoclusters of known concentration was centrifuged at 10 000 rpm for 10 min at 4 °C. FAAS measurements were conducted on the supernatant.

Hyperspectral Characterization of Nanoclusters in Solution: Microscope slides were submerged in a warm, aqueous gelatin solution (3% w/v) for 10 min. The slides were removed from the gelatin, and 10 μL of a dilute nanocluster dispersion (∼0.01 mg/mL) was placed on the gelatin-coated slide and covered with a coverslip. The gelatin was allowed to cool for 2 h to allow the nanoparticles to solidify into the gelatin. Hyperspectral images were acquired under the same conditions as described below for cell studies.

Cellular Studies of Nanocluster Disassembly: The cells were cultured in a 12-well plate in phenol-free DMEM media (Gibco, Grand Is-

land, NY) supplemented with 5% fetal bovine serum (Hyclone, Logan, UT) and antibiotics (Gibco, Grand Island, NY) and incubated at 37 °C in a 5% CO_2 environment for 1 week. The nanoclusters were filtered through a 0.45 μm filter (Corning, Corning, NY) spun down and resuspended in DMEM medium and, then, were added to each well with cells (0.4 mg per well). Incubation of the cells with the nanoclusters occurred over 24 h, after which the excess of the nanoparticles was removed and the cells were allowed to proliferate to 96 or 168 h time points. The cells were washed three times in 0.01 M phosphate buffered saline (PBS), harvested, and centrifuged at 110g for 3 min. The supernatant was discarded. The cells were resuspended in 10 μL of PBS, placed on a microscope slide, and imaged using a combination of dark-field reflectance and hyperspectral imaging. Dark-field reflectance microscopy images of the cells and nanoclusters were taken with a Leica DM6000 upright microscope, and the hyperspectral images were acquired with a PARISS spectral imager (Lightform Inc.). The same 20×, 0.5 NA objective and a 75 W Xe light source were used for both imaging modalities. The hyperspectral system was calibrated using a standard wavelength calibration lamp (low pressure Hg, Lightform, Inc.). All hyperspectral spectra from cells were normalized by the spectrum of the Xe excitation light source on a pixel by pixel basis. RGB images were taken with a Q-imaging Retiga EXi CCD camera with color LCD attachment. Images were white balanced with a Spectralon (Labsphere, North Sutton, NH), and the acquisition settings were chosen such that all samples were acquired under identical conditions.

For the TEM studies of the cells, approximately 3×10^4 macrophage cells were seeded overnight on Aclar Embedding Film (Electron Microscopy Sciences, Hatfield, PA). All samples for TEM imaging were treated identically and were run in parallel to the samples used for optical imaging. At each time point, the cells were fixed in a 1% glutaraldehyde and 1% paraformaldehyde solution for 1 h at room temperature and then washed three times in PBS. Subsequently, cells were stained with 2% osmium tetroxide in water for 10 min and washed for 10 min in water. The sample was then dehydrated using increasing ratios of ethanol to acetone solutions and finally embedded in an epoxy−acetone mixture and allowed to bake at 60 °C for 24 h. Ultrathin sections were sliced using a Leica Ultracut microtome (Leica, Deerfield, IL) and imaged with the Tecnai G2 TEM at a voltage of 80 kV.

Supporting Information Available: Proposed mechanism for nanocluster formation; determination of the nanocluster extinction cross section; and additional figures. This material is available free of charge *via* the Internet at http://pubs.acs.org.

REFERENCES AND NOTES

1. Hirsch, L. R.; Stafford, R. J.; Bankson, J. A.; Sershen, S. R.; Rivera, B.; Price, R. E.; Hazle, J. D.; Halas, N. J.; West, J. L. Nanoshell-Mediated Near-Infrared Thermal Therapy of Tumors under Magnetic Resonance Guidance. *Proc. Natl. Acad. Sci. U.S.A.* **2003**, *100*, 13549–13554.
2. Oldenburg, S. J.; Averitt, R. D.; Westcott, S. L.; Halas, N. J. Nanoengineering of Optical Resonances. *Chem. Phys. Lett.* **1998**, *288*, 243–247.

3. Loo, C.; Lowery, A.; Halas, N.; West, J.; Drezek, R. Immunotargeted Nanoshells for Integrated Cancer Imaging and Therapy. *Nano Lett.* **2005**, *5*, 709–711.

4. Huang, X.; El-Sayed, I. H.; Qian, W.; El-Sayed, M. A. Cancer Cell Imaging and Photothermal Therapy in the Near-Infrared Region by Using Gold Nanorods. *J. Am. Chem. Soc.* **2006**, *128*, 2115–2120.

5. Skrabalak, S. E.; Chen, J.; Au, L.; Lu, X.; Li, X.; Xia, Y. Gold Nanocages for Biomedical Applications. *Adv. Mater.* **2007**, *19*, 3177–3184.

6. Chen, J.; Saeki, F.; Wiley, B. J.; Cang, H.; Cobb, M. J.; Li, Z.-Y.; Au, L.; Zhang, H.; Kimmey, M. B.; Li, X.; Xia, Y. Gold Nanocages: Bioconjugation and Their Potential Use as Optical Imaging Contrast Agents. *Nano Lett.* **2005**, *5*, 473–477.

7. Ma, L. L.; Feldman, M. D.; Tam, J. M.; Paranjape, A. S.; Cheruku, K. K.; Larson, T. A.; Tam, J. O.; Ingram, D. R.; Paramita, V.; Villard, J. W.; Clarke, G. D.; Jenkins, J. T.; Asmis, R.; Sokolov, K.; Chandrasekar, B.; Milner, T. E.; Johnston, K. P. Small Multifunctional Nanoclusters (Nanoroses) for Targeted Cellular Imaging and Therapy. *ACS Nano* **2009**, *3*, 2686–2696.

8. Jain, P. K.; Lee, K. S.; El-Sayed, I. H.; El-Sayed, M. A. Calculated Absorption and Scattering Properties of Gold Nanoparticles of Different Size, Shape, and Composition: Applications in Biological Imaging and Biomedicine. *J. Phys. Chem. B* **2006**, *110*, 7238–7248.

9. Chen, J. Y.; Wang, D. L.; Xi, J. F.; Au, L.; Siekkinen, A.; Warsen, A.; Li, Z. Y.; Zhang, H.; Xia, Y. N.; Li, X. D. Immuno Gold Nanocages with Tailored Optical Properties for Targeted Photothermal Destruction of Cancer Cells. *Nano Lett.* **2007**, *7*, 1318–1322.

10. Ji, X. J.; Shao, R. P.; Elliott, A. M.; Stafford, R. J.; Esparza-Coss, E.; Bankson, J. A.; Liang, G.; Luo, Z. P.; Park, K.; Markert, J. T.; Li, C. Bifunctional Gold Nanoshells with a Superparamagnetic Iron Oxide-Silica Core Suitable for Both MR Imaging and Photothermal Therapy. *J. Phys. Chem. C* **2007**, *111*, 6245–6251.

11. Lee, S. E.; Liu, G. L.; Kim, F.; Lee, L. P. Remote Optical Switch for Localized and Selective Control of Gene Interference. *Nano Lett.* **2009**, *9*, 562–570.

12. Schipper, M. L.; Iyer, G.; Koh, A. L.; Cheng, Z.; Ebenstein, Y.; Aharoni, A.; Keren, S.; Bentolila, L. A.; Li, J. Q.; Rao, J. H.; Chen, X. Y.; Banin, U.; Wu, A. M.; Sinclair, R.; Weiss, S.; Gambhir, S. S. Particle Size, Surface Coating, and PEGylation Influence the Biodistribution of Quantum Dots in Living Mice. *Small* **2009**, *5*, 126–134.

13. Betancourt, T.; Brown, B.; Brannon-Peppas, L. Doxorubicin-Loaded PLGA Nanoparticles by Nanoprecipitation: Preparation, Characterization and *In Vitro* Evaluation. *Nanomedicine* **2007**, *2*, 220–232.

14. Kooi, M. E.; *et al.* Accumulation of Ultrasmall Superparamagnetic Particles of Iron Oxide in Human Atherosclerotic Plaques Can Be Detected by *In Vivo* Magnetic Resonance Imaging. *Circulation* **2003**, *107*, 2453–2458.

15. Almutairi, A.; Akers, W. J.; Berezin, M. Y.; Achilefu, S.; Frechet, J. M. J. Monitoring the Biodegradation of Dendritic Near-Infrared Nanoprobes by *In Vivo* Fluorescence Imaging. *Mol. Pharmaceutics* **2008**, *5*, 1103–1110.

16. Choi, H. S.; Liu, W.; Misra, P.; Tanaka, E.; Zimmer, J. P.; Ipe, B. I.; Bawendi, M. G.; Frangioni, J. V. Renal Clearance of Quantum Dots. *Nat. Biotechnol.* **2007**, *25*, 1165–1170.

17. Arruebo, M.; Fernandes-Pacheko, R.; Ibarra, M. R.; Santamaria, J. Magnetic Nanoparticles for Drug Delivery. *Nano Today* **2007**, *2*, 22–32.

18. Peer, D.; Karp, J. M.; Hong, S.; Farokhzad, O. C.; Margalit, R.; Langer, R. Nanocarriers as an Emerging Platform for Cancer Therapy. *Nat. Nanotechnol.* **2007**, *2*, 751–760.

19. Alivisatos, P. The Use of Nanocrystals in Biological Detection. *Nat. Biotechnol.* **2004**, *22*, 47–52.

20. Anker, J. N.; Hall, W. P.; Lyandres, O.; Shah, N. C.; Zhao, J.; Van Duyne, R. P. Biosensing with Plasmonic Nanosensors. *Nat. Mater.* **2008**, *7*, 442–453.

21. Lewinski, N.; Colvin, V.; Drezek, R. Cytotoxicity of Nanoparticles. *Small* **2008**, *4*, 26–49.

22. Xu, L.; Guo, Y.; Xie, R.; Zhuang, J.; Yang, W.; Li, T. Three-Dimensional Assembly of Au Nanoparticles Using Dipeptides. *Nanotechnology* **2002**, *13*, 725–728.

23. Selvakannan, P. R.; Mandal, S.; Phadtare, S.; Pasricha, R.; Sastry, M. Capping of Gold Nanoparticles by the Amino Acid Lysine Renders Them Water-Dispersible. *Langmuir* **2003**, *19*, 3545–3549.

24. Lim, I. I. S.; Ip, W.; Crew, E.; Njoki, P. N.; Mott, D.; Zhong, C.-J.; Pan, Y.; Zhou, S. Homocysteine-Mediated Reactivity and Assembly of Gold Nanoparticles. *Langmuir* **2007**, *23*, 826–833.

25. Basu, S.; Pal, T. Glutathione-Induced Aggregation of Gold Nanoparticles: Electromagnetic Interactions in a Closely Packed Assembly. *J. Nanosci. Nanotechnol.* **2007**, *7*, 1904–1910.

26. Ofir, Y.; Samanta, B.; Rotello, V. M. Polymer and Biopolymer Mediated Self-Assembly of Gold Nanoparticles. *Chem. Soc. Rev.* **2008**, *37*, 1814–1825.

27. Boal, A. K.; Ilhan, F.; DeRouchey, J. E.; Thurn-Albrecht, T.; Russell, T. P.; Rotello, V. M. Self-Assembly of Nanoparticles into Structured Spherical and Network Aggregates. *Nature* **2000**, *404*, 746–748.

28. Gindy, M. E.; Panagiotopoulos, A. Z.; Prud'homme, R. K. Composite Block Copolymer Stabilized Nanoparticles: Simultaneous Encapsulation of Organic Actives and Inorganic Nanostructures. *Langmuir* **2008**, *24*, 83–90.

29. Grabar, K. C.; Allison, K. J.; Baker, B. E.; Bright, R. M.; Brown, K. R.; Freeman, R. G.; Fox, A. P.; Keating, C. D.; Musick, M. D.; Natan, M. J. Two-Dimensional Arrays of Colloidal Gold Particles: A Flexible Approach to Macroscopic Metal Surfaces. *Langmuir* **1996**, *12*, 2353–2361.

30. Chow, M. K.; Zukoski, C. F. Gold Sol Formation Mechanisms: Role of Colloidal Stability. *J. Colloid Interface Sci.* **1994**, *165*, 97–109.

31. Sakai, T.; Alexandridis, P. Mechanism of Gold Metal Ion Reduction, Nanoparticle Growth and Size Control in Aqueous Amphiphilic Block Copolymer Solutions at Ambient Conditions. *J. Phys. Chem. B* **2005**, *109*, 7766–7777.

32. Kumar, S.; Harrison, N.; Richards-Kortum, R.; Sokolov, K. Plasmonic Nanosensors for Imaging Intracellular Biomarkers in Live Cells. *Nano Lett.* **2007**, *7*, 1338–1343.

33. DeVries, G. A.; Brunnbauer, M.; Hu, Y.; Jackson, A. M.; Long, B.; Neltner, B. T.; Uzun, O.; Wunsch, B. H.; Stellacci, F. Divalent Metal Nanoparticles. *Science* **2007**, *315*, 358–361.

34. Khlebtsov, B.; Zharov, V.; Melnikov, A.; Tuchin, V.; Khlebtsov, N. Optical Amplification of Photothermal Therapy with Gold Nanoparticles and Nanoclusters. *Nanotechnology* **2006**, *17*, 5167–5179.

35. Aaron, J.; Nitin, N.; Travis, K.; Kumar, S.; Collier, T.; Park, S. Y.; Jose-Yacaman, M.; Coghlan, L.; Follen, M.; Richards-Kortum, R.; Sokolov, K. Plasmon Resonance Coupling of Metal Nanoparticles for Molecular Imaging of Carcinogenesis *In Vivo*. *J. Biomed. Opt.* **2007**, *12*, 034007/1–034007/11.

36. Sokolov, K.; Follen, M.; Aaron, J.; Pavlova, I.; Malpica, A.; Lotan, R.; Richards-Kortum, R. Real Time Vital Imaging of Pre-Cancer Using Anti-EGFR Antibodies Conjugated to Gold Nanoparticles. *Cancer Res.* **2003**, *63*, 1999–2004.

37. Larson, T. A.; Bankson, J.; Aaron, J.; Sokolov, K. Hybrid Plasmonic Magnetic Nanoparticles as Molecular Specific Agents for MRI/Optical Imaging and Photothermal Therapy of Cancer Cells. *Nanotechnology* **2007**, *18*, 325101.

38. Troutman, T. S.; Barton, J. K.; Romanowski, M. Biodegradable Plasmon Resonant Nanoshells. *Adv. Mater.* **2008**, *20*, 2604–2608.

39. Vasir, J. K.; Labhasetwar, V. Biodegradable Nanoparticles for Cytosolic Delivery of Therapeutics. *Adv. Drug Delivery Rev.* **2007**, *59*, 718–728.